J. Meas. Sci. Instrum., 2025, 16(4): 505-514.
DOI: 10.62756/jmsi.1674-8042.2025049
http://jmsi.publish.founderss.cn/
jmsi@nuc.edu.cn

Application of soft sensor modeling based on SSA-CNN-LSTM in solar thermal power collection subsystem

LU Xiaojuan[1*], ZHANG Yaohui[1], FAN Duojin[2], KONG Linggang[2], ZHANG Zhiyong[2]

1. School of Automation Electrical Engineering, Lanzhou Jiaotong University, Lanhzou 730070, China;
2. Research Institute of Photothermal Energy Storage, Lanzhou Jiaotong University, Lanhzou 730070, China

***Corresponding author:** LU Xiaojuan (luxj@mail.lzjtu.cn)

Received: August 8, 2024 **Revised:** September 17, 2024 **Accepted:** October 28, 2024

Abstract: To address the stochasticity and nonlinearity of solar collector power systems, a soft sensor prediction model with a hybrid convolutional neural network (CNN) and long short-term memory network (LSTM) was constructed, and the hyperparameter optimization of the hybrid neural network (CNN-LSTM) was carried out by using the sparrow search algorithm (SSA). The model utilized the powerful feature extraction and non-linear mapping capabilities of deep learning to effectively handle the complex relationship between input and target variables. The batch normalization technique was used to speed up the training and improve the stability of the soft-sensing model, and the random discard technique was used to prevent the soft-sensing model from overfitting. Finally, the mean absolute error (MAE) was used to assess the accuracy of the soft sensor model predictions. This study compared the proposed model with soft sensor prediction models like Bp, Elman, CNN, LSTM, and CNN-LSTM, using dynamic thermal performance data from the solar collector field of the molten salt linear Fresnel photovoltaic demonstration power plant. The deep learning-based soft sensor model outperformed the other models according to the experimental data. Its coefficients of determination (namely R^2) are higher by 6.35%, 8.42%, 5.69%, 6.90%, and 3.67%, respectively. The accuracy and robustness have been significantly improved.

Key words: soft sensor modeling; linear Fresnel collector subsystem; collector field outlet temperature; deep learning; sparrow search algorithm

0 Introduction

Photothermal energy is becoming increasingly important in the realization of a carbon-peak and carbon-neutral strategic energy system[1]. Renewable energy expansion is not only a means of accelerating the energy transition but also a model for social renewable energy development[2,3].

One renewable energy source that can provide a consistent and dependable power output, flexible adjustment, and a sizable contribution to the basic power load is solar thermal power generation[4]. China has also invested heavily in the production of solar thermal electricity. The advantages of linear Fresnel over other concentrated kinds of solar thermal power generation include a low wind load coefficient, flexible construction, and a lower investment. It has the potential to be a significant contributor to solar thermal power generation. Nevertheless, the advent of this novel energy source is contingent upon the intrinsic properties of solar energy. In the event of insufficient light, the temperature of the molten salt medium will not reach the requisite working temperature, thereby preventing the steam parameters from meeting the required specifications. Consequently, the efficiency of steam turbine power generation will be significantly diminished. Therefore, for the linear Fresnel photothermal power station to operate efficiently, the temperature of the melting salt at the exit of the linear Fresnel collector circuit must be accurately predicted and consistently controlled[5,6].

The application of artificial neural networks[7-9] and optimization algorithms[10,11] in prediction has been the subject of much research. Tiago et al. have proposed a sophisticated management technique for fluid overheating in photovoltaic power plants[12]. By regulating the fluid velocity, the temperature was maintained within the normal range, and the solar collector was defocused when the temperature exceeds the maximum safety value. Raj et al. investigated the impact of artificial roughness factors on the thermal performance of solar collectors[13]. The creation of an artificial neural network model was guided by the

findings. Paulo et al. presented an optimal management approach for solar power gathering[14]. Through a data simulation carried out in Brazil, the effectiveness of the suggested control approach has been verified, with the predicted yearly revenue reaching up to 13.5% of the possible advantages. To increase system stability, Liang et al. presented a predictive control approach based on the Kalman filter[15]. Zhang et al. proposed an RBF neural network temperature prediction model based on the k-means algorithm[16]. According to the simulation findings, this model predicted the output temperature of the linear Fresnel solar collector field more accurately. Aamer et al. proposed a prediction error-based power prediction method using a grey box neural network (GBNN)[17]. Based on the data from a PV system, the evaluation metrics were found to be of good quality. The efficacy of the proposed prediction scheme was substantiated. Lu et al. proposed a sliding mode predictive control strategy that exhibited superior performance compared to MPC and SMPC[18]. The strategy had greater robustness and immunity to interference. Liu et al. proposed an Elman neural network and a prediction model using improved particle swarm optimization as a means of stabilizing wind energy output, given the inherent randomness and volatility of wind speed[19]. Pataro et al. presented an algorithm for stochastic predictive management for a genuine solar energy thermal power plant based on the chance constrained (CC) formulation[20]. The experimental results demonstrated that, in contrast to the deterministic strategy, the CC-PMNPC consistently reduced the temperature threshold extrapolation. In light of the above, there is a paucity of studies investigating the utilization of deep learning in conjunction with soft sensor modeling.

This study presented a soft sensing model based on a hybrid neural network, CNN-LSTM, for forecasting the outlet temperature of a linear Fresnel collector loop. The intricate nature of solar thermal power systems precluded the possibility of measuring certain key parameters in real time, which in turn gave rise to inaccuracies in the prediction of the outlet temperature of the collector field. The methodology presented in this paper aimed to facilitate the automatic discovery of intricate relationships between inputs and outputs through the utilization of multi-level non-linear transformations. This process differed from the conventional approach of soft sensor modeling. This resulted in a model that was more relevant to solar thermal power systems. Finally, to confirm the effectiveness and accuracy of the proposed method, this study evaluated and compared the performance of five soft sensor models in predicting the collector field output temperature.

1 Linear Fresnel solar thermal power generation systems

1.1 Analysis of linear Fresnel solar thermal power system

The structure diagram of the linear Fresnel solar thermal power generation system is presented in Fig. 1. The linear Fresnel solar collector field is comprised of multiple linear Fresnel collector branches. The linear Fresnel collector system comprises a primary reflector and a secondary concentrator. The secondary concentrator and the vacuum collector tube collectively constitute the absorption component of the system.

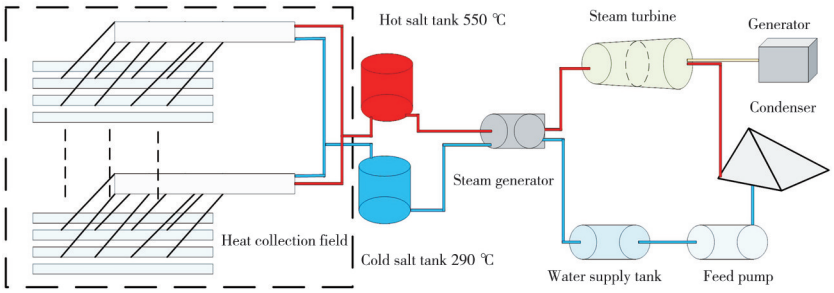

Fig. 1 Structure of molten salt linear Fresnel solar thermal power system

After primary reflection, the tracking control system allows the main reflecting surface to target sunlight over the secondary concentrator by tracking the sun's location in real time. Following the secondary reflection of the CPC, the solar light is concentrated efficiently in the vacuum collector tube. The medium then heats up rapidly, and the solar energy is converted and stored.

1.2 Dynamic model of linear Fresnel collector subsystems

The linear Fresnel collector system has a collector loop length of 1 100 m. The remaining temperature sensor sites are positioned at the center of the collector loop, with the intake and exit respectively serving as the temperature measurement points. By utilizing the concepts of heat

conduction, convection, and radiation transmission, the energy conservation equations for the glass outer tube, glass inner tube, stainless steel heat pipe, and molten salt medium within the vacuum collecting tube are determined to be expressed as

$$\frac{T_{ge}-T_a}{R_1}+\frac{T_{ge}-T_a}{R_2}=\frac{T_{gi}-T_{ge}}{R_3}, \tag{1}$$

$$\frac{T_{gi}-T_{ge}}{R_3}=\frac{T_r-T_{gi}}{R_4}, \tag{2}$$

$$Q_{sb}=\frac{T_r-T_{gi}}{R_4}+\frac{T_r-T_f}{R_5}, \tag{3}$$

$$\frac{T_r-T_f}{R_5}=CM\triangle T=C\rho V(T_r-T_{in}). \tag{4}$$

The energy absorbed by the inner tube of the vacuum collector tube, the energy absorbed by the molten salt medium, and the total heat loss of the system are

$$Q_{sb}=IS\eta, \tag{5}$$

$$Q_{loss}=\frac{T_r-T_{gi}}{R_4}=\frac{T_{gi}-T_{ge}}{R_3}=\frac{T_{ge}-T_a}{R_1}+\frac{T_{ge}-T_a}{R_2}, \tag{6}$$

$$Q_{system}=Q_{loss}+C\rho V(T_r-T_{in}). \tag{7}$$

A detailed explanation of the above parameters is shown in Table 1.

Table 1 Model parameter list

Variant	Description
T_{ge}/℃	Outer wall temperature of vacuum collector tube glass tube
T_a/℃	Ambient temperature
T_{gi}/℃	Inner wall temperature of a vacuum collector glass tube
T_r/℃	Temperature of a metal tube inside the vacuum collector tube
T_f/℃	Temperature of fluid in a metal tube
T_{in}/℃	Inlet medium temperature of the collector circuit
R_1-R_5/(K•W^{-1})	Thermal resistance of heat transfer between different components
Q_{sb}/J	Energy is absorbed by the metal inner tube of the vacuum collector tube
C/(J•(kg•℃)$^{-1}$)	Specific heat of molten salt
M /kg	Molten salt quality
V /m^3	Volume of molten salt medium
$\triangle T$/℃	Temperature difference
ρ/(kg•m^{-3})	Density of molten salt
I /(W•m^{-2})	Direct solar irradiation
S /m^2	Collector branch condenser mirror area
η/%	Comprehensive efficiency of the heat collection system

2 CNN-LSTM based soft sensor modelling

2.1 Data processing

In the field of solar energy research, the inherent variability of solar irradiation intensity presents challenges that can significantly affect the outcomes of analyses and models. To address this issue, we applied k-means clustering to the solar irradiation intensity data, segmenting the yearly dataset into four distinct categories. This categorization aimed to mitigate the impact of randomness by allowing us to focus on representative days that exemplified each category's characteristics.

Fig.2 delineates the clustering outcomes, highlighting the four categories derived from the k-means algorithm. By selecting the most representative day for each category based on frequency, we enhanced the reliability and robustness of our results, ultimately contributing to a more nuanced understanding of solar irradiation patterns in the region.

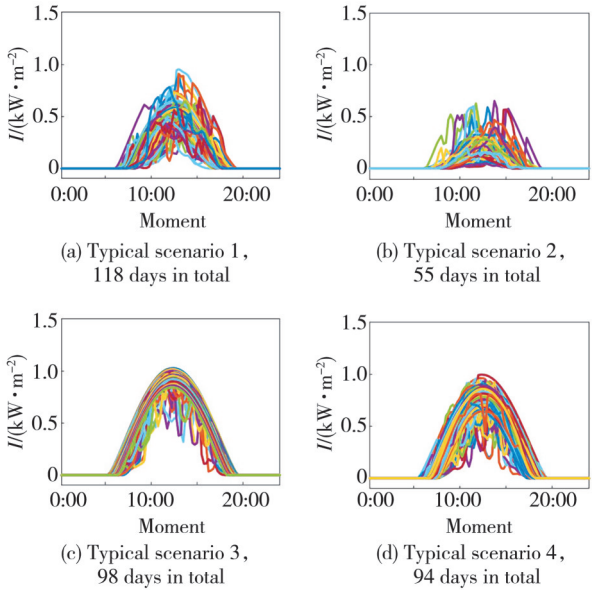

Fig. 2 Clustering results for annual solar irradiation intensity. Different coloured curves in graphs represent different numbers of days

Due to the involvement of various influencing factors in many aspects, the initial data show significant differences. Therefore, standardizing the original data is of vital importance for improving the predictive efficiency of the network.

$$X_n=\frac{x_i-\mathrm{mean}(x)}{x_{max}-x_{min}}, \tag{8}$$

where X_n is the standardized data, x_i is a sample of the original data, and $\mathrm{mean}(x)$ is the mean of the raw data.

2.2 Selection of auxiliary variables and dominant variables

The auxiliary variables were chosen based on the results of the field study, pertinent literature, and Eqs.(1) to (7). The intensity of the sun's rays, wind speed, ambient temperature, atmospheric humidity, molten salt input

temperature of the collector circuit, and inlet flow of the collector circuit are the last auxiliary factors.

The soft sensor modeling expression of the heat collection system is

$$\boldsymbol{Y}_{(t+1)}=f(\boldsymbol{I}_{(t)},\boldsymbol{T}_{\mathrm{in}(t)},\boldsymbol{T}_{\mathrm{a}(t)},\boldsymbol{Q}_{\mathrm{in}(t)},\boldsymbol{H}_{\mathrm{u}(t)},\boldsymbol{W}_{(t)}). \tag{9}$$

2.3 Model construction

Through the convolutional layer and pooling layer, a CNN is a machine learning technique that collects spatial and frequency domain information about features. When processing time series data, a LSTM can capture long-term dependencies in an efficient manner.

The complex interactions among wind speed, atmospheric humidity, other environmental factors, and the collector field's output temperature can be captured by the LSTM model.

The combination of CNN and LSTM units results in a hybrid neural network that exhibits the spatial feature lifting capability of CNN and retains the long-term dependence of LSTM in dealing with time series. This hybrid network is more comprehensive in its processing capabilities.

The CNN-LSTM network is shown in Fig.3.

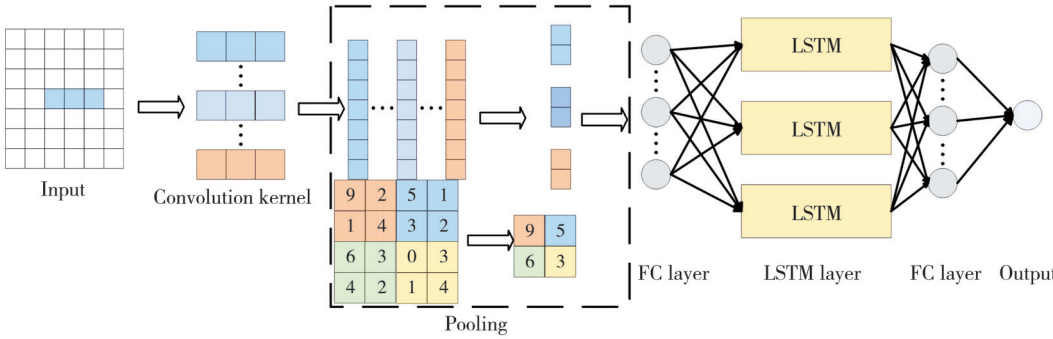

Fig. 3 CNN-LSTM network

The input feature matrix $\boldsymbol{X}$ of the test is set as

$$\boldsymbol{X}=\left[\boldsymbol{I}_{(t)},\boldsymbol{T}_{\mathrm{in}(t)},\boldsymbol{T}_{\mathrm{a}(t)},\boldsymbol{Q}_{\mathrm{in}(t)},\boldsymbol{H}_{\mathrm{u}(t)},\boldsymbol{W}_{(t)}\right], \tag{10}$$

where the training sample $\boldsymbol{X}$ is a matrix of order $m\times 6$; the $\boldsymbol{I}_{(t)}$, $\boldsymbol{T}_{\mathrm{in}(t)}$, $\boldsymbol{T}_{\mathrm{a}(t)}$, $\boldsymbol{Q}_{\mathrm{in}(t)}$, $\boldsymbol{H}_{\mathrm{u}(t)}$, $\boldsymbol{W}_{(t)}$ represent column matrices of solar direct radiation, the molten salt inlet temperature of the collector circuit, environmental temperature, the inlet flow rate of the collector circuit, atmospheric humidity, and wind speed. They can be expressed as

$$\boldsymbol{I}(t)=\begin{bmatrix}I_{11}\\I_{21}\\\vdots\\I_{(m-1)1}\\I_{m1}\end{bmatrix},\quad \boldsymbol{T}_{\mathrm{in}(t)}=\begin{bmatrix}T_{\mathrm{in}11}\\T_{\mathrm{in}21}\\\vdots\\T_{\mathrm{in}(m-1)1}\\T_{\mathrm{in}m1}\end{bmatrix}, \tag{11}$$

$$\boldsymbol{T}_{\mathrm{a}(t)}=\begin{bmatrix}T_{\mathrm{a}11}\\T_{\mathrm{a}21}\\\vdots\\T_{\mathrm{a}(m-1)1}\\T_{\mathrm{a}m1}\end{bmatrix},\quad \boldsymbol{Q}_{\mathrm{in}(t)}=\begin{bmatrix}Q_{\mathrm{in}11}\\Q_{\mathrm{in}21}\\\vdots\\Q_{\mathrm{in}(m-1)1}\\Q_{\mathrm{in}m1}\end{bmatrix}, \tag{12}$$

$$\boldsymbol{H}_{\mathrm{u}(t)}=\begin{bmatrix}H_{\mathrm{u}11}\\H_{\mathrm{u}21}\\\vdots\\H_{\mathrm{u}(m-1)1}\\H_{\mathrm{u}m1}\end{bmatrix},\quad \boldsymbol{W}_{(t)}=\begin{bmatrix}W_{11}\\W_{21}\\\vdots\\W_{(m-1)1}\\W_{m1}\end{bmatrix}. \tag{13}$$

In this paper, the value of m is set to 300, which corresponds to the use of 300 sets of data as test sets for the purpose of predicting the future outlet temperature of the collector field. The input vector to the model is a matrix comprising 6 300 rows and 1 column.

Step 1 After preprocessing, the data enters the convolution layer and moves on the input data with a 3×1 convolution kernel for convolution. The convolution data is weighted to extract different features of the input data and map to

$$x_k^l=f\left(\sum_{i=1}^{N}x_i^{l-1}*w_{ik}^l+b_k^l\right), \tag{14}$$

where x_k^l represents the kth convolution map of the lth layer, N represents the number of input convolution maps, and $*$ represents the convolution operation. Meanwhile, w_{ik}^l represents the weight of the kth convolution kernel in the l layer for the ith operation and represents the bias of the l layers corresponding to the kth convolution kernel.

Step 2 Input the features extracted by the first step of convolution into the pooling layer. In this paper, the maximum pooling method is used to take the maximum value from x_k^l to x_{k+m-1}^l, and the pooling operation is performed with m as the step size in the sequence x.

$$\hat{x}_k^l=\max\left(x_k^l{:}x_{k+m-1}^l\right). \tag{15}$$

Step 3 The pooled feature vector is employed as the input of the LSTM via the fully connected layer. The two functions of the input gate work in conjunction to convert the input vector from 0 to 1, thereby determining whether

to add memory cells and subsequently judging whether to retain the value of the previous moment through the forgetting gate.

$$\begin{cases} i_t = \sigma(\boldsymbol{W}_i h_t - 1 + \boldsymbol{U}_i x_t + \boldsymbol{b}_i), \\ \tilde{C}_t = \tanh(\boldsymbol{W}_c h_t - 1 + \boldsymbol{U}_c x_t + \boldsymbol{b}_c), \\ f_t = \sigma(\boldsymbol{W}_f h_{t-1} + \boldsymbol{U}_f x_t + \boldsymbol{b}_f), \\ C_t = f_t * C_t - 1 + i_t * \tilde{C}_t, \\ O_t = \sigma(\boldsymbol{W}_o[h_t - 1, x_t] + \boldsymbol{b}_o), \\ h_t = O_t * \tanh(C_t), \end{cases} \tag{16}$$

where i_t is t, the time input door control, x_t is the input, σ is the sigmoid function, $\boldsymbol{W}$ is cycle weight, $\boldsymbol{U}$ is input weight, $\boldsymbol{b}$ is biased, $\tilde{C}_t$ is input the cell state value at t, h_{t-1} is the weight coefficient of the previous moment, and f_t indicates that the gate value is ignored at time t, C_t is t moment memory cell state value, C_{t-1} is the memory cell state value at the previous moment, * is the standard product of the matrix, and O_t is the output value of the gate control unit at the current time.

Step 4 The data output from step 3 is passed through the dropout layer to prevent overfitting of time series data.

Step 5 The output prediction value of the fully connected layer is

$$\hat{\boldsymbol{Y}}_{(t+1)} = \begin{bmatrix} Y_{11} \\ Y_{21} \\ \vdots \\ Y_{(m-1)1} \\ Y_{m1} \end{bmatrix}. \tag{17}$$

In conclusion, this is the soft sensor model of CNN-LSTM, and its computational complexity is contingent upon the structure of the convolutional and LSTM layers. The computational complexity of the entire model is 2 589 M. In practice, it will also be influenced by other factors, such as the alteration of the batch size and so forth.

2.4 Optimization models

In the case of neural network models, the traditional approach is to set the hyperparameters required by the network according to experience, with the optimal array being obtained through numerous experiments. However, during the process of experimentation, there is often an issue of overfitting and local optimal solutions. The performance of SSA was compared with GWO, PSO, and GSA. SSA performed better[21]. Given this, the CNN-LSTM soft sensor prediction model of the linear Fresnel collection subsystem is subjected to hyper-parameter optimization in this study using the SSA.

2.4.1 Sparrow optimization algorithm

The goal of the SSA is to mimic the foraging and anti-predatory tendencies of sparrows.

To optimize the model, it is essential to simulate the foraging behavior of sparrows. Matrix $\boldsymbol{X}$ is the position representation of the sparrow.

$$\boldsymbol{X} = \begin{bmatrix} x_{11} & x_{12} & \cdots & x_{1d} \\ x_{21} & x_{22} & \cdots & x_{2d} \\ \vdots & \vdots & \vdots & \vdots \\ x_{n1} & x_{n2} & \cdots & x_{nd} \end{bmatrix}, \tag{18}$$

where d is the optimization model's parameter dimension and n is the quantity of sparrows.

The fitness value of each sparrow is represented by

$$\boldsymbol{F}_x = \begin{bmatrix} \boldsymbol{f}([x_{11} & x_{12} & \cdots & x_{1d}]) \\ \boldsymbol{f}([x_{21} & x_{22} & \cdots & x_{2d}]) \\ \vdots & \vdots & \vdots & \vdots \\ \boldsymbol{f}([x_{n1} & x_{n2} & \cdots & x_{nd}]) \end{bmatrix}. \tag{19}$$

The location update of the discoverer is

$$X_{ij}^{t+1} = \begin{cases} X_{ij}^t \exp\left(\dfrac{-i}{\alpha iter_{\max}}\right), & R_2 < ST, \\ X_{ij}^t + \boldsymbol{QL}, & R_2 \geqslant ST, \end{cases} \tag{20}$$

where X_{ij}^t represents the position information of the ith sparrow in the jth dimension at the tth iteration, $\alpha \in (0, 1]$, and $\boldsymbol{Q}$ is a random number that obeys the standard normal distribution. Meanwhile, $\boldsymbol{L}$ is a $1 \times d$ matrix, and R_2 and ST represent early warning value and safety value in turn.

The followers go to the resource location according to the signal sent by the discoverer, and the follower location is updated by

$$X_{ij}^{t+1} = \begin{cases} Q \exp\left(\dfrac{X_{\text{worst}}^t - X_{ij}^t}{i^2}\right), & i > \dfrac{n}{2}, \\ X_p^{t+1} + \left| X_{ij}^t - X_p^{t+1} \right| \boldsymbol{A}^+ \boldsymbol{L}, & \text{otherwise}, \end{cases} \tag{21}$$

where X_{worst}^t represents the worst position of the individual in the population in the tth iteration, X_p^{t+1} denotes the best position in the population after the $t+1$ iteration, and $\boldsymbol{A}$ is a matrix of $1 \times d$ whose elements are 1 or -1.

The location update of the alert is

$$X_{ij}^{t+1} = \begin{cases} X_{\text{best}}^t + \beta \left| X_{ij}^t - X_{\text{best}}^t \right|, & f_i > f_h, \\ X_{ij}^t + K\left[\dfrac{\left| X_{ij}^t - X_{worst}^t \right|}{(f_i - f_l) + \varepsilon}\right], & f_i = f_h, \end{cases} \tag{22}$$

where X_{best}^t represents the best position found by the alert after t iterations, β is a normal distribution random number with a mean of 0 and a variance of 1, $K \in [-1, 1]$, and ε is a constant that is the smallest but not 0. Meanwhile, f_i represents the fitness value of the individual after t

iterations, while f_h and f_l represent the highest fitness value and the lowest fitness value of the individual in the current sparrow population, respectively.

2.4.2 Hyperparameter optimization

The model was evaluated in terms of its complexity, convergence speed, and propensity to overfit. There are four hyperparameters set in this study. The hyperparameters that need to be tuned for the hybrid neural network are the quantity of neurons, the beginning learning rate, and the L2 regularization coefficient. The optimal neural network size falls between [10, 100], the optimized initial learning rate falls between [0.001, 0.1], the optimized number of convolution kernels falls between [8, 128], and the optimized L2 regularization coefficient falls between [0, 1]. For the optimization process, the previously discussed SSA is used. There are some parameters needed for the optimization process. The discoverer represents 20% of the population; there are ten iterations, a safety threshold of 0.8, and an optimization dimension of four.

Finally, after optimizing the parameters of the entire model, it was determined that the input layer neurons of the CNN-LSTM were 6, the output layer neurons were 1, the convolution kernel size was 3×1, the convolution kernels was 32 , the step size was 1, the maximum quantity of iterations was 1 000, the quantity of neurons was 27, the optimal initial learning rate was 0.002 823 2, and the optimal L2 regularization coefficient was 2.744 1e-06.

The flow chart model is presented in Fig.4.

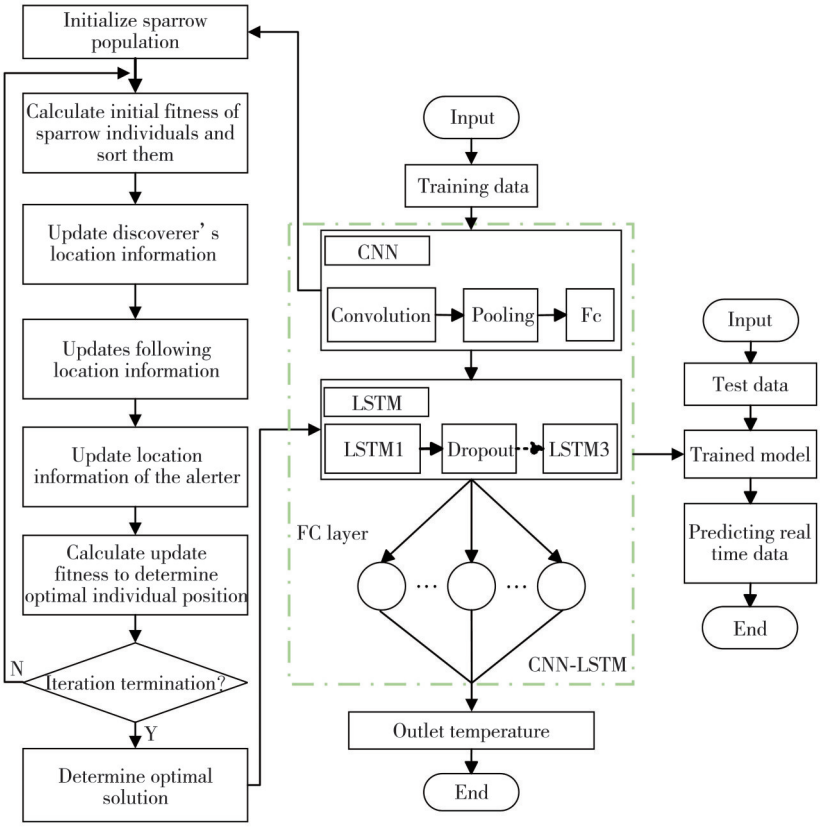

Fig. 4 Flow chart of hybrid SSA-CNN-LSTM model

3 Experiment

3.1 Data source

We selected the 118 feature groups with the highest frequency of occurrence for this study. The field data used in this paper was collected from the molten salt linear Fresnel solar thermal demonstration power plant. Fig.5 illustrates the raw data obtained. Out of a total of 600 data sets, we allocated 300 sets for training and the remaining 300 sets for testing.

3.2 Model performance indicators

Once the model is established, it is necessary to define an evaluation index to assess the value and accuracy of the model. In this paper, the performance of the model is evaluated using three statistical indicators: mean absolute percentage error (MAPE), mean absolute error (MAE), and coefficient of determination (R^2).

The expressions for these indicators are

$$MAPE = \frac{1}{N}\sum_{i=1}^{N}\frac{|\hat{y}_i - y_i|}{y_i}, \tag{23}$$

$$MAE=\frac{1}{N}\sum_{i=1}^{N}\left|\hat{y}_i-y_i\right|, \tag{24}$$

$$R^2=1-\frac{\sum_{i=1}^{N}(\hat{y}_i-y_i)^2}{\sum_{i=1}^{N}(\hat{y}_i-\bar{y})^2}, \tag{25}$$

where N represents the amount of test set samples, y_i and $\hat{y}_i$ represent the actual value and predicted value of the ith test set sample, respectively, and $\bar{y}$ represents the mean value of the actual value.

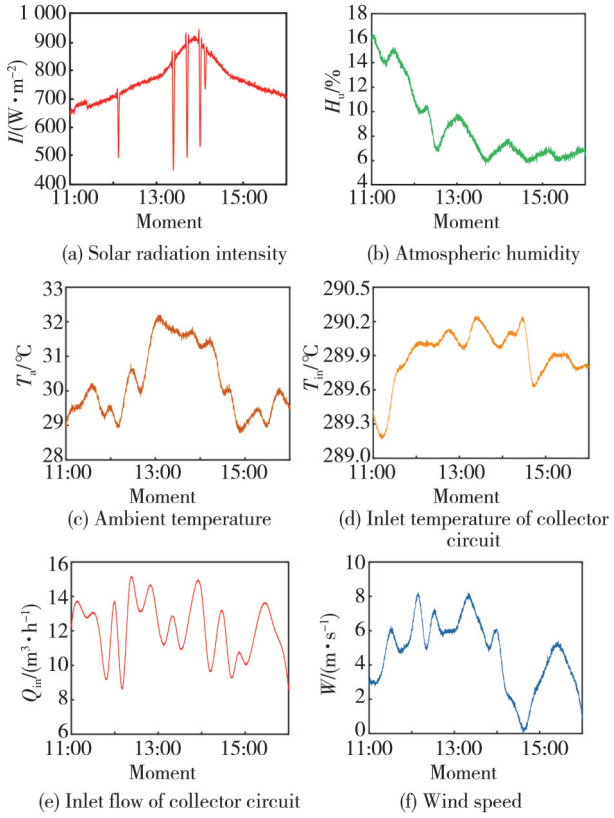

Fig. 5 Experiment raw data

3.3 Performance comparison of different models

This work builds four models of the Bp soft sensor model, the Elman soft sensor model, the CNN soft sensor model, and the LSTM soft sensor model for comparison analysis to show the superiority of the SSA-CNN-LSTM soft sensor model. To further improve the model's performance, several activation functions are also used for the training function, dropout layer parameter configuration, and ideal soft sensor model.

Fig.6 illustrates the predicted outlet temperature of the collector field for five distinct soft sensor models. The CNN-LSTM soft sensor model exhibits the highest degree of fit with the actual outlet temperature of the collector field. The CNN-LSTM soft sensor model exhibits the most favorable prediction performance among the soft sensor models.

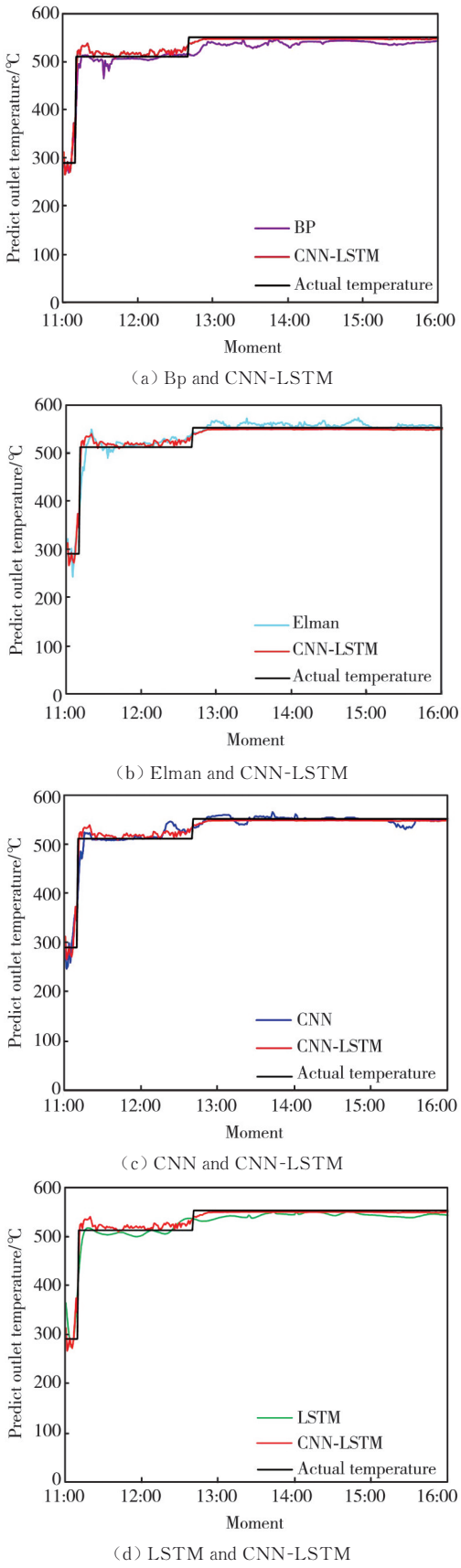

Fig. 6 Prediction curves of outlet temperature for five soft sensor models

Fig. 7 depicts the relative error curves of the outlet temperature of the collector field predicted by five

distinct soft sensor models in comparison to the actual outlet temperature. It shows that between 11: 00 and 13: 00, there is a particularly noticeable difference between the expected and actual numbers. However, compared to other single soft sensor models, the CNN-LSTM soft sensor model shows less error fluctuation, which gives the hybrid model a greater level of prediction accuracy. Between 13:00 and 16:00, the error is more stable, but the proposed method in this paper is even more stable.

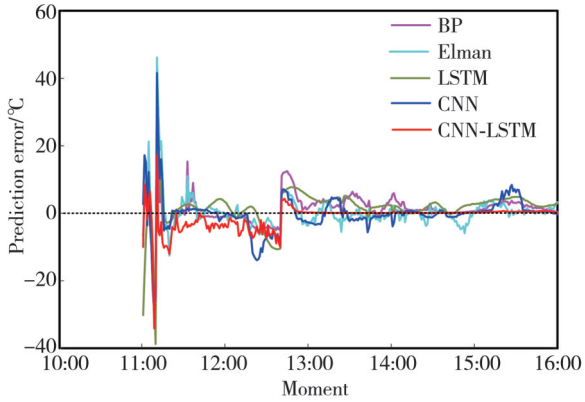

Fig. 7 Relative error curves of outlet temperature prediction for five soft sensor models

Table 2 illustrates that the CNN-LSTM soft sensor model and the Bp soft sensor model exhibit reductions of 31.4% and 53.3%, respectively, in comparison to the Elman soft sensor model. Concurrently, the R^2 value has been enhanced by 3.02% and 5.09%, respectively. A comparison of the results indicates that the incorporation of a CNN into a LSTM neural network facilitates the extraction of local features from data, thereby enhancing the accuracy of the model. When comparing MEA to the LSTM and single CNN soft sensor models, R^2 is increased by 2.36% and 3.33%, respectively, whereas reductions of 26.8% and 33.1%, respectively, are observed.

Table 2 Comparison of outlet temperature errors for five soft sensor models

Soft sensor model	MAE	MAPE/%	R^2
Bp	7.35	1.46	0.918 2
Elman	8.57	1.83	0.897 5
CNN	7.03	1.42	0.924 8
LSTM	7.44	1.55	0.915 1
CNN-LSTM	5.59	1.14	0.948 4

As illustrated in Fig.8, the impact of varying parameter settings on the model is evident. The highest accuracy of the model is observed when the dropout layer parameter is set to 0.1. When the parameter is set to 0.4, the model exhibits the lowest accuracy. The impact of distinct training algorithms on the model is that the Adam algorithm is 14% more effective than the Sgdm algorithm. Consequently, it is recommended that different model training algorithms are selected in accordance with this finding. The model's predictive power is greatly influenced by the selection of the activation function. For this paradigm, the ideal activation function is represented by the tanh function.

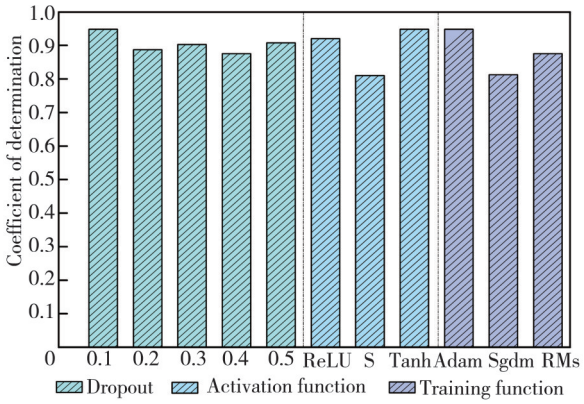

Fig. 8 Effect of different dropout parameters, activation functions, and training algorithms on model

3.4 Comparison of optimized and unoptimized models

Fig. 9 illustrates that the optimized soft sensor model exhibits a greater degree of fit with the actual situation than the unoptimized soft sensor model. Fig.10 illustrates the comparison between the optimized soft sensor model and the unoptimized soft sensor model. The principal fluctuations are concentrated between step changes with very little fluctuation during the steady state phase, but it is evident that the error curve of the optimized soft sensor model exhibits less variability and is relatively more stable.

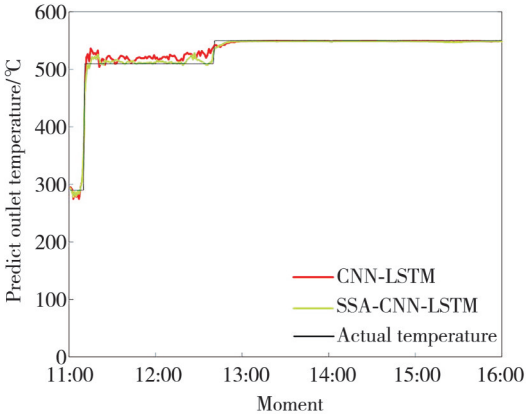

Fig. 9 Prediction curves of outlet temperature for optimized and unoptimized soft sensor models

Table 3 reflects that the MAE of the optimized soft sensor model decreases by 40.60% and the R^2 increases by 3.67% compared with the non-optimized soft sensor model. This indicates the significance of the relevant parameters for the soft sensor model. Moreover, identifying the optimal parameter combination for the soft sensor model can further

enhance its stability and accuracy.

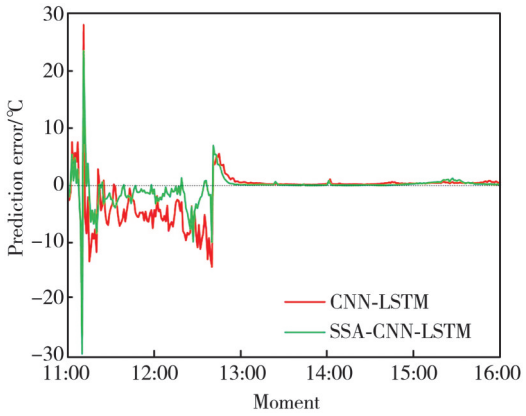

Fig. 10 Prediction error curves of outlet temperature for optimized and unoptimized soft sensor models

Table 3 Comparison of outlet temperature errors for optimized and unoptimized soft sensor models

Soft sensor model	MAE	MAPE/%	R^2
CNN-LSTM	5.59	1.14	0.948 4
SSA-CNN-LSTM	3.32	0.75	0.985 1

In conclusion, the SSA-CNN-LSTM soft sensor model exhibits superior prediction ability in comparison to several other single soft sensor models, and demonstrates a higher degree of fit with the actual situation.

4 Conclusions

The hybrid neural network-based soft sensor model created in this study provides a solution to the problem of monitoring the collector field's temperature at the outlet in the actual field.

1) The wind speed and environmental temperature in the actual data are normalized, thereby unifying the dimensions of the original meteorological data and enhancing the training speed of the soft sensor prediction model.

2) The CNN-LSTM software sensor prediction model enhances the model's ability to extract features from various dimensions and enables adaptive learning as well as modification of the memory unit state. Compared with the CNN software sensor model, the R^2 value has increased by 2.36% and 3.33%, respectively, while MAE has decreased by 26.8% and 33.1%, respectively. The LSTM software sensor model performs even better.

3) In the training process of a CNN-LSTM, this paper compares different activation functions, dropout layer parameters, and training algorithms to obtain the final results, which are tan, 0.1, and Adam, respectively. The sparrow search method is employed to determine the ideal neuron count as 27. And 0.002 823 2 is the starting learning rate, 2.7441e-06 is the regularization coefficient, and 32 is the amount of convolution kernels. Training models are now more effective.

Acknowledgement

This work was supported by National Natural Science Foundation of China (No. 52266012), Gansu Province College Industry Support Plan Project (No.2022CYZC-34), Gansu Province Major Science and Technology Special Project (Nos. 20ZD7GF011, 22ZD6GA063) and Jiuquan City Science and Technology Programme Project (No.2023CA3058).

Declaration of conflicting interests

The authors have no conflict of interests related to this publication.

References

[1] ZHOU J Z, JI W H, CAO X L, et al. A current perspective on the renewable energy hydrogen production process. Journal of Thermal Science, 2023, 32(2): 542-596.

[2] PARANDEH K, BAGHERI A, JADID S. Optimal day-ahead dynamic pricing of grid-connected residential renewable energy resources under different metering mechanisms. Journal of Modern Power Systems and Clean Energy, 2023, 11(1): 168-178.

[3] YANG X X, CAI B, XUE Y S. Review on optimization of nuclear power development: a cyber-physical-social system in energy perspective. Journal of Modern Power Systems and Clean Energy, 2022, 10(3): 547-561.

[4] HU Z G, JIN Z Y. Opportunities and challenges of solar thermal power generation in China under the background of an energy transformation strategy. Solar Energy, 2019(11): 11-17.

[5] WANG R D, MA J, WANG C L, et al. Progress of linear Fresnel concentrator heat collection system. Infrared and Laser Engineering, 2021, 50(11): 20210452.

[6] GAO X B, LIAO C H, LI G. Study on control strategy and variable load rate of linear Fresnel solar power station. Thermal Power Generation, 2024, 53(5): 47-55.

[7] SU T, ZHAO J B, PEI Y S, et al. Probabilistic physics-informed graph convolutional network for active distribution system voltage prediction. IEEE Transactions on Power Systems, 2023, 38(6): 5969-5972.

[8] LI J J, ZHANG C H, SUN B. Two-stage hybrid deep learning with strong adaptability for detailed day-ahead photovoltaic power forecasting. IEEE Transactions on Sustainable Energy, 2023, 14(1): 193-205.

[9] ALIBERTI A, FUCINI D, BOTTACCIOLI L, et al. Comparative analysis of neural networks techniques to forecast global horizontal irradiance. IEEE Access, 2021, 9: 122829-122846.

[10] ZHAO J Y, CHI Y, ZHOU Y T. Short-term load forecasting based on SSA-LSTM model. Advanced Technology of Electrical Engineering and Energy, 2022, 41(6): 71-79.
[11] JI Y Q, YAN Y B, HE P, et al. CNN-LSTM short-term load forecasting based on the K-Medoids clustering and grid method to extract load curve features. Power System Protection and Control, 2023, 51(18): 81-93.
[12] DE ARAÚJO ELIAS T, DA COSTA MENDES P R, NORMEY-RICO J E. Hybrid predictive controller for overheating prevention of solar collectors. Renewable Energy, 2019, 136: 535-547.
[13] KUMAR R, NADDA R, KUMAR S, et al. Influence of artificial roughness parametric variation on thermal performance of solar thermal collector: an experimental study, response surface analysis and ANN modelling. Sustainable Energy Technologies and Assessments, 2022, 52: 102047.
[14] BIAZETTO P H F, DE ANDRADE G A, NORMEY-RICO J E. Development of an optimal control strategy for temperature regulation and thermal storage operation of a solar power plant based on Fresnel collectors. IEEE Transactions on Control Systems Technology, 2023, 31(3): 1149-1164.
[15] LU X J, LIANG Z P. Application of model predictive control based on Kalman filter in solar collector field of solar thermal power generation. Energy Engineering, 2021, 118(4): 1171-1183.
[16] ZHANG Z Y, LU X J, KONG L G, et al. Predicting molten salt temperature at the circuit outlet of linear Fresnel heat collector using K-means combined with RBF neural network. Transactions of the Chinese Society of Agricultural Engineering, 2021, 37(3): 213-222.
[17] SHAH A, AHMED K, HAN X. A novel prediction error-based power forecasting scheme for real PV systems using the PVUSA model: a grey box-based neural network approach. IEEE Access, 2021, 9: 87196-87206.
[18] LU X J, SUN P, FAN D J. Application of sliding mode predictive control in a solar thermal power generation collector subsystem. Journal of Applied Science and Engineering, 2023, 26(10): 1481-1489.
[19] LIU W, XUE F F, GAO Y S, et al. Wind-speed forecasting model based on DBN-Elman combined with improved PSO-HHT. Global Energy Interconnection, 2023, 6(5): 530-541.
[20] PATARO I M L, GIL J D, AMERICANO DA COSTA M V, et al. A stochastic nonlinear predictive controller for solar collector fields under solar irradiance forecast uncertainties. IEEE Transactions on Control Systems Technology, 2024, 32(1): 99-111.
[21] XUE J K, SHEN B. A novel swarm intelligence optimization approach: sparrow search algorithm. Systems Science & Control Engineering, 2020, 8(1): 22-34.

基于SSA-CNN-LSTM的软测量建模在太阳能热发电集热子系统中的应用研究

路小娟[1*], 张耀辉[1], 范多进[2], 孔令刚[2], 张志勇[2]

1. 兰州交通大学 自动化与电气工程学院, 甘肃 兰州 730070;
2. 兰州交通大学研究院光热储能综合能源系统工程研究中心, 甘肃 兰州 730070

摘　要： 针对太阳能热发电集热系统随机性和非线性的特点，构建了SSA-CNN-LSTM软测量预测模型。该模型利用深度学习强大的特征提取和非线性映射能力，有效地处理了输入变量与目标变量之间复杂的关系。运用批量归一化技术来加速软测量模型的训练和提高稳定性，同时利用随机丢弃防止软测量模型过拟合。用混合神经网络（CNN-LSTM）软测量模型对处理后的数据进行训练预测，并利用麻雀优化算法优化混合神经网络（CNN-LSTM）的超参数。最后，利用平均绝对误差（MEA）等来评判软测量模型预测的准确性。本研究以熔盐线性菲涅尔式光热示范电站太阳能集热场动态热性能数据来验证该文提出的模型，并且和BP，Elman，CNN，LSTM，CNN-LSTM软测量预测模型比较。实验结果表明，所构建的基于深度学习的软测量模型比其他几种模型决定系数（R^2）提高了6.35%，8.42%，5.69%，6.90%，3.67%，在精度、鲁棒性等方面取得显著提升。

关键词： 软测量建模；线性菲涅尔集热子系统；集热场出口温度；深度学习；麻雀搜索算法

引用格式： LU Xiaojuan, ZHANG Yaohui, FAN Duojin, et al. Application of soft sensor modeling based on SSA-CNN-LSTM in solar thermal power collection subsystem. Journal of Measurement Science and Instrumentation, 2025, 16(4): 505-514. DOI: 10.62756/jmsi.1674-8042.2025049